

Calibration of the first XMM Flight Mirror Module

I - Image Quality

Ph. Gondoin^a, B. Aschenbach^b, M. Beijersbergen^a, R. Egger^b
F. Jansen^a, Y. Stockman^c, J.P. Tock^c

^a European Space Research and Technology Center, 2200 AG Noordwijk zh, the Netherlands

^b Max-Planck Institute fur Extraterrestrische Physik, 8046 Garching, Germany

^c Centre Spatial de Liege, B-4031 Liege, Belgium

ABSTRACT

The High Throughput X-ray Spectroscopy Mission (XMM) is a “Cornerstone” Project in the ESA long-term Programme for Space Science. The satellite observatory uses three grazing incidence mirror modules coupled to reflection grating spectrometers and X-ray CCD cameras. Each XMM mirror module consists of 58 Wolter I mirrors which are nested in a coaxial and cofocal configuration. The calibration of the mirror system includes the development of a representative numerical model and its validation against extensive calibration tests performed on ground at the CSL and PANTER test facilities. The present paper describes the calibration of the X-ray image quality of the first XMM flight mirror module.

Keywords: XMM, X-ray astronomy, Wolter I telescope, grazing incidence optics

1. INTRODUCTION

The X-ray Multi-Mirror Observatory XMM¹ is a “Cornerstone” project in the ESA long-term programme for space science due for launch in August 1999. The primary scientific objective of XMM is to perform high throughput spectroscopy of cosmic x-ray sources over a broad band of energies ranging from 0.1 keV to 10 keV. The XMM model payload includes three grazing incidence mirror modules^{2,3} combined with three CCD imaging cameras (EPIC)^{4,5} and two reflection grating spectrometers (RGS)⁶. An optical monitor (OM)⁷ permits simultaneous monitoring of x-ray sources in the optical and UV spectral range.

With the spectroscopic capability of the mirror modules associated to the EPIC and RGS instrument, XMM will improve our understanding of hot astrophysical plasma. The interpretation of this next generation data requires that calibration of the telescopes and payload is performed to a high level of accuracy. For instance, in order to derive the differential emission measure distribution of optical thin plasma as a function of temperature, as well as for deriving elemental abundance, we need to know relative line intensities and the continuum to an accuracy of 5 to 10 percent. Thus the accuracy on the mirror module effective area and encircled energy function at all energy should be 2 - 3 percent throughout the 0.1 to 10 keV passband.

The absence of cosmic x-ray sources which could serve as in-orbit calibration standards prevents an in orbit calibration of the mirror modules to a high level of accuracy. The effective area and encircled energy function of the mirrors have therefore to be calibrated on ground. The situation is further complicated since on-ground testing cannot be performed in fully representative operation conditions. Indeed, full aperture X-ray test data gathered at the MPE long beam Panter Facility is compromised by the finite source distance. In such tests a large fraction of the reflecting surfaces of the mirror shells are not used. Full aperture data for a source at infinity is available from the CSL vertical test facility but only at EUV wavelengths. In order to overcome these difficulties and to satisfy the calibration requirements, a comprehensive and reliable numerical model of the XMM mirror system is needed. This model shall generate the telescope calibration database by extrapolating on-ground tests to in-orbit operation conditions and by interpolating between the finite number of measurement points. The on-ground calibration recipe therefore includes the realization of a mirror module simulator and its validation by on-ground EUV and x-ray tests. The present paper describes how these tasks were completed for the calibration of the image quality of the first XMM flight mirror module.

2. DESCRIPTION OF AN XMM FLIGHT MIRROR MODULE

In order to deliver the high throughput of photons with the required spatial resolution, a Wolter I design⁸ was selected for each of the three XMM mirror modules (see Figure 1). This design is driven by the requirement of obtaining the highest possible effective collecting area over a wide band of energies. Particular emphasis has been given on the region around 7 keV, in which the K lines of the astrophysically important iron appear. Because of this high energy requirement the mean mirror grazing incidence angle is limited to 30 arcmin. The total length of the telescope is imposed by the launcher so that the focal length is 7.5 meters. Similarly, the maximum diameter of each of the three adjacent telescopes must not exceed 70 cm to be compatible with the shroud diameter of the launcher.

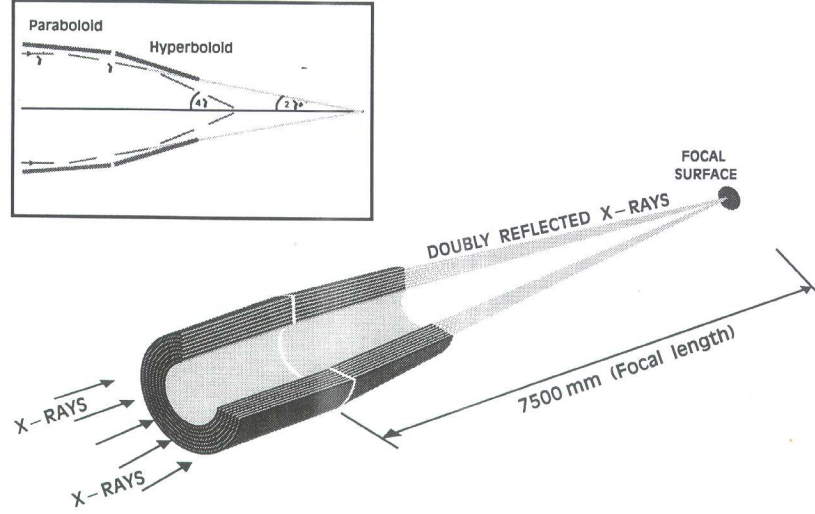


Figure 1. optical design of an XMM mirror module

Table 1. optical characteristics of an XMM mirror module

focal length	7500 mm
outer mirror radius	350 mm
inner mirror radius	153 mm
axial mirror length	600 mm
outer mirror thickness	1.07 mm
inner mirror thickness	0.47 mm
minimum packing distance	1 mm
mirror substrate material	Nickel
reflective coating	Gold
number of mirrors per module	58

Based on mass constraints and on the performance of the selected nickel electroforming technology⁹, a 0.47 mm wall thickness for the smallest mirror diameter of 300 mm was baselined. The thickness variation then increases linearly with shell diameter in order to guarantee sufficient stiffness. The thickness of the 700 mm diameter mirror equals 1.07 mm. A minimum radial separation of 1 mm between adjacent shells was adopted. Each mirror shell of the Wolter telescope consists of a paraboloid and an associated hyperboloid which are replicated together in one piece in order to facilitate alignment and integration. Since the effective collecting area decreases with smaller shell

radius, the inner shells become less and less effective and the associated throughput gain has to be traded against the effort of production. An optimum at 8 keV is reached for an innermost shell diameter of 150 mm and a total of 58 shells per module.

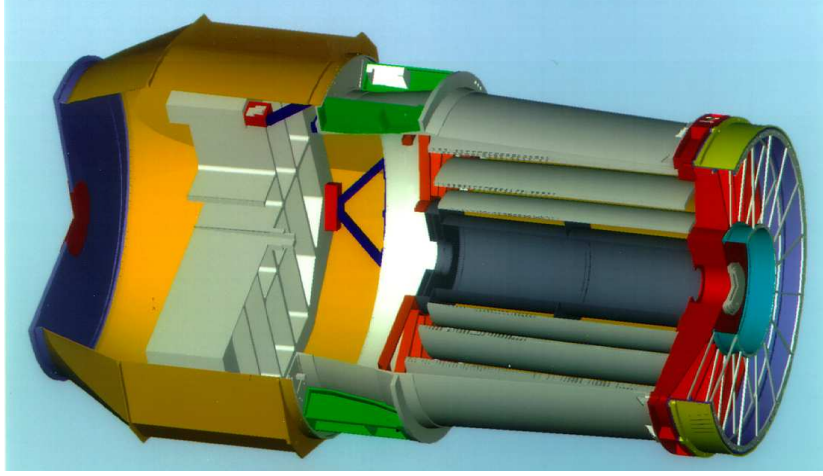


Figure 2. mechanical layout of an XMM mirror module

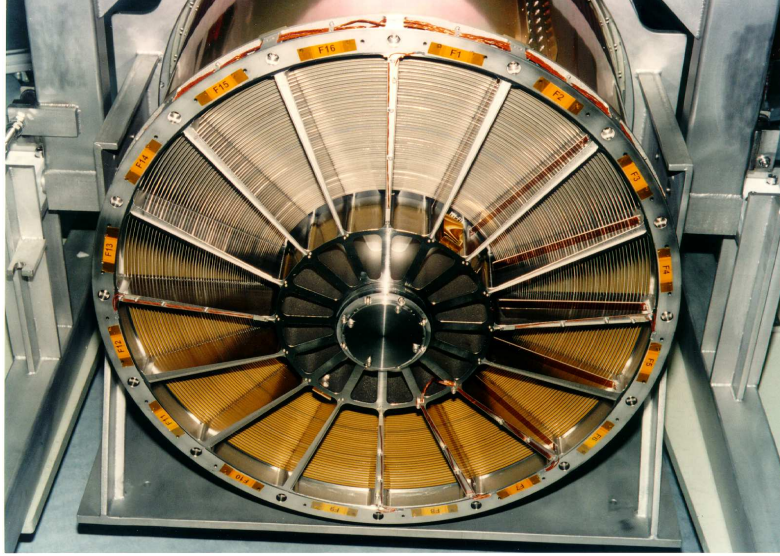


Figure 3. entrance aperture of the FM1 XMM mirror module

The mechanical layout of an XMM mirror module is described in figure 2. The 58 Wolter I mirrors are bounded on their entrance aperture to the 16 spokes of a single spider. The spider is connected to the support platform of the spacecraft via an interface structure consisting on an outer cylinder and an interface ring. The outer cylinder is prolonged by an adaptor ring which connects the mirror module to an exit thermal baffle. On two of the three mirror modules, this adaptor ring also interface the mirror module to a reflection grating assembly. An electron deflector is located at the exit aperture of the mirror module. It consists of a spider having sixteen spokes which carry magnets. The magnets produce a circumferential magnetic field which diverts soft energy electrons reflected by

the mirrors away from the focal plane detectors. Two sieve plates consisting each of 58 annular apertures are located respectively 85 and 145 mm in front of the mirror entrance aperture. This two sieves baffle acts as a collimator and reduces the amount of straylight in the detector field of view.

3. THE MIRROR MODULE SIMULATOR

3.1. The ray-tracing code

The mirror simulator which shall generate calibration datafiles consists of a ray tracing code and a numerical model of the mirror module. The ray tracing code performs a ray-trace of the mirror module to obtain a conventional point spread function. The intersection point of each incident ray with a mirror section, i.e. the paraboloid or hyperboloid of a Wolter I mirror is calculated. Each intersection point is characterized by its cylindrical coordinates and the local surface normal. These are used to calculate the direction of the specular reflected ray. After each reflection, a deviation from specular reflection is implemented according to a predefined distribution which simulates surface scattering. This distribution weighs the number of rays as a function of their scattered angle according to the Rayleigh-Rice vector perturbation theory¹⁰.

$$I(\beta) = I_{specular}(\beta) + I_{scatter}(\beta)$$

with:

$$I_{specular}(\beta) = R(\alpha) \cdot [1 - (4 \cdot \pi \cdot \sigma \cdot \sin(\alpha) / \lambda)^2] \cdot \delta(\beta - \alpha)$$

and

$$I_{scatter}(\beta) = \sqrt[3]{R(\alpha) \cdot R(\beta)} \cdot 16 \cdot (\pi^2 / \lambda^3) \cdot \sin(\alpha) \cdot \sin^2(\beta) \cdot PSD(f)$$

α is the incident grazing angle onto the mirror, $R(\alpha)$ the mirror surface reflectivity and $PSD(f)$ the monodimensional power spectral density of the mirror surface. The relation between the surface spatial frequency f and the angle of scattering β is given by the grating equation applied to the first order of diffraction.

$$f = (\cos(\beta) - \cos(\alpha)) / \lambda$$

Each individual ray carries an intensity coefficient to account for scattering and reflectivity loss. It is then ray-traced through the remainder of the optical system using the same procedure. The gold surface reflectivity is calculated from tables of refraction indices using the Fresnel equation for a semi-infinite medium. In the x-ray range above 100 eV, the 1993 Henke table¹¹ is used initially as updated based on new absorption coefficient data to improve the description of the gold M absorption edge. Below 100 eV, we used the refraction index table from D.W. Lynch and W.R. Hunter¹². Grazing incidence reflectivity from the Nickel backside of the mirrors and from the spider spokes is negligible in the x-ray range because of the high roughness of these surfaces.

The monodimensional scatter distribution is a useful approximation which is only valid for grazing incidence mirrors. For such mirrors indeed, the ellipsoidal scatter pattern is very much elongated in the tangential direction by a factor $1/\alpha$ which equals about 100 for the XMM mirrors. The validity range of the first order scattering theory can be estimated from the power spectral density of the XMM mirrors. An estimate of the Rayleigh limit between geometrical and scattering behaviour gives surface period values included between one mm and two cm in the soft x-ray range. For an ideal Wolter I geometry of the XMM mirror, aperture diffraction effects are negligible in the x-ray range while fully dominating in the visible range. First order scattering and slope errors play therefore a major role in the x-ray domain. Hence, the mirror figuring errors and the surface roughness measured in the workshop enable us to simulate the response of the XMM mirrors with a high accuracy in the 0.1 keV to 10 keV XMM spectral band.

3.2. The numerical model of the mirror module

The numerical model of the mirror modules incorporates the opto-mechanical design of the 58 mirrors and simulates the vignetting of the x-ray beam by the entrance spider and the exit magnetic deflector of the mirror module. The XMM Wolter I mirrors are produced by nickel electroforming onto aluminium mandrels. During the mass production of the flight model mirrors, different measuring devices¹³ are used for characterization of the mirrors surface and geometry before final integration onto the spider of the mirror module. The numerical model of an XMM mirror module incorporate these workshop metrology data as described below.

3.2.1. Low-frequency circumferential profiles

After replication and separation from its mandrel progenitor, each mirror is measured using a screening device. The screening device performs circumferential profile measurements at 6 axial positions of each individual mirror shell. In order to avoid any surface deformation of the mirrors under their own weight, the shells are suspended at 16 locations by hooks connected via springs and miniature dynamometers to 16 actuators. An isostatic support of the thin floppy mirror shells is obtained by adjusting the displacements of the 16 actuators such that identical forces are obtained and read on the 16 dynamometers. The screening device measurement accuracy is of the order of a micron for a specification on the mirror shell out-of-roundness of less than 150 microns. All mirror shells of the first flight mirror modules have been measured using the screening device to acquire information about the figure errors of the mirrors. This results in low-frequency data, of the order of the size of the mirrors which provide information on the mirror out-of-roundness and taper error between paraboloid and hyperboloid. The screening device data are preprocessed in the workshop. The deformation is expanded into an orthogonal set of Fourier-Legendre polynomials. Individual coefficients of this expansion can be associated in lowest order with tilt, decenter, taper error and out-of-roundness. These mirror deformations are ray traced in the numerical model using the measured set of Fourier-Legendre polynomials.

3.2.2. Mid-frequency axial profiles

The surface of the flight mirrors is also characterized by a 3-D measuring machine. This high precision measuring device is equipped with a non-contacting optical probe which allows to measure the axial profile of individual mirror shells. Mirrors are suspended on a mirror suspension device during measurements as described above. A typical measurement set consists of four axial profiles with 200 data points. The information obtained in each point of the profile are its three dimensional coordinates within a predefined mirror reference frame. The power spectral density (PSD) of the axial profiles is noise limited to less than 10^{-4} mm^{-3} so that characterization of the paraboloid or hyperboloid profiles of the mirror by this measuring device is effective in the 10mm - 300 mm spatial wavelength range. Slope errors are lower than a few arcsec on most of the mirror surface. Large slope errors are only seen at the

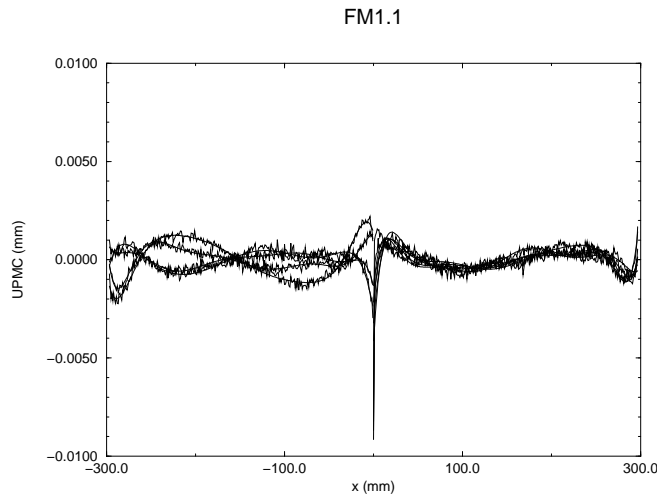


Figure 4. polynomial fit of figuring errors of the largest FM1 mirror

edge of the mirrors and at the parabola to hyperbola intersection plane. The roll-off deformation at the intersection plane are replication of the roll-off induced by the polishing tool on the mandrel. Roll-off deformation at the edges of the mirror are due to internal stress release after replication. In order to filter the real mirror deformation from the instrument measurement noise, a 9th order polynomial fit is applied to each measured profile. Fourier transform of the profiles indicate that the measuring noise dominates at surface periods lower than a few centimeters and are filtered in a satisfying way by the polynomial fit. The 9th order polynomial description of the axial profile errors of the mirrors is therefore included in the mirror numerical model. The simulator interpolate linearly the deformation between the four measured azimuths. Measurements and 9th order polynomial fit of the four axial profiles of the largest FM1 mirror are shown on Figure 4.

3.2.3. High-frequency surface roughness

The surface roughness of the mandrels and mirrors is measured using a commercial microscope profiler. This profiler is a Michelson interferometer that incorporates a microscope objective and the surface to be measured. It operates in phase shifting interferometry using an internal reference mirror mounted on a piezoelectric transducer¹⁴. A CCD collects the interference patterns corresponding to the three different phase shifts between the interfering beams. A computer programme reconstructs these data into a three dimensional image of the measured surface. Ten CCD lines are extracted from each image corresponding to ten different axial profiles. After correction from profile tilt and offset, a one dimensional estimate of the power spectral density is calculated for each CCD line. Measurements are performed at four different azimuth angle on the paraboloid and hyperboloid section of each mandrel and mirror. The power spectral densities (PSD) of all CCD lines and images are then averaged to provide a good statistical description of the surface micro-roughness. The microscope is equipped with a 40 magnification objective which leads to a spatial wavelength coverage of 0.2 mm to 0.003 mm on the mirror surface. Use of a 2.5 magnification objective allows to extend the surface coverage up to a 3.2 mm spatial wavelength. Figure 6 shows the power spectral densities of the smallest FM1 mirror measured at different location on the mirror parabola and hyperbola surface. The power spectral density averaged on the surface matched accurately a broken PSD derived from x-ray angle resolved scatter measurements (see Section 4.2). The surface power spectral density of the mirror module is calculated by averaging on each mirror the eight azimuthal PSD and then by averaging the 58 mirrors PSDs. This low noise power spectral density is included in the numerical model of the mirror module. Wing scattering is then simulated by the ray-tracing code using the first order scattering theory.

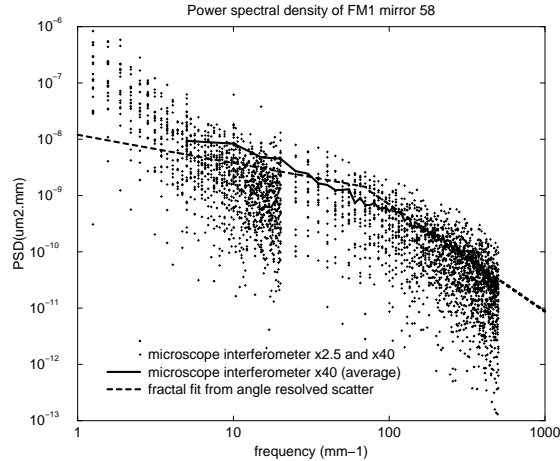


Figure 5. power spectral density of mirror 58

3.2.4. Alignment

After successful measurements by the metrology instruments, the flight quality mirror shells are integrated onto the front spider of the mirror module using a vertical optical bench. The vertical optical bench provides a collimated

beam with 800 mm diameter. The individual mirror shells are aligned by optimization of the single reflection hyperboloid focus which is very sensitive to misalignment tilt giving coma. By using a rotating Hartmann mask combined with intra and extra focal imaging, the relative coordinate of the best focus position of each single shell can be determined. Contacting probes also provide the mirror position with respect to the spider. This information is used to simulate the core of the telescope point spread function which is sensitive to the misalignment of the individual mirror shells.

The last operation performed on the mirror module is the integration of the front x-ray baffle which is made of two sieve plates. Each sieve plate has 58 concentric annular apertures which have been precisely manufactured. They are carefully aligned in front of the annular entrance aperture of the 58 mirror shells. The sieves prevent single hyperbola reflections from rays emitted by bright x-ray sources located at off-axis angle larger than 20 arcmin. During manufacturing, the dimensions of the sieve annular grooves have been measured with one micron accuracy. This information is implemented into the mirror module software model and is used to calculate the off-axis vignetting function and the straylight rejection efficiency of each mirror module.

4. CALIBRATION TESTS OF THE FM1 MIRROR MODULE

4.1. Measurements of the EUV Image Quality

Full aperture illumination tests are performed at the CSL vertical facility¹⁵ which provides a full aperture vertical collimated beam. An electron cyclotron resonance EUV source which emits in the HeI and HeII lines at 58 and 30 nm illuminates a pinhole placed at the focus of a vertical Cassegrain telescope. The platinum coated primary and secondary mirrors provide a parallel beam of 800 mm diameter. The X-ray mirror module is located above the Cassegrain telescope in the vertical collimated beam. It focuses the beam through aluminium filters on a thinned back side illuminated CCD. The overall set-up is located in a vertical vacuum chamber.

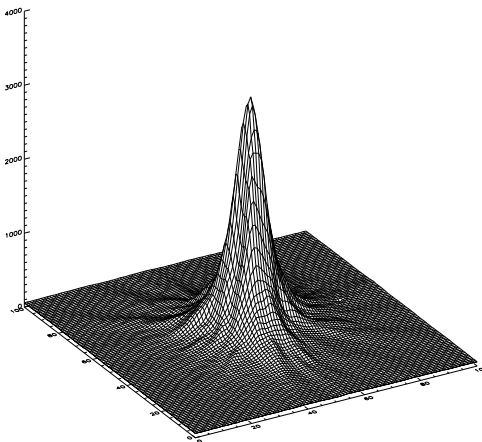


Figure 6. measured PSF of XMM FM1 mirror module at 58nm

The CSL image of the EUV point spread function (PSF) of the FM1 mirror module is shown on Figure 6. The PSF exhibits a slight triangular shape which was induced during integration by an imperfect flatness of the mechanical interface between the spider and the outer cylindrical structure. Since mirror shape metrology is performed before integration, the resulting mirror deformations are not implemented in the numerical model. This effect does not influence the simulation accuracy of the azimuthally averaged PSF. Simulation of the CCD measurements of the on-axis EUV PSF were conducted using the FM1 numerical model with screening device data, measured axial profiles, decenter and thicknesses of the mirrors. The measured and simulated encircled energy functions of FM1 mirror module response are given in Figure 7. The results are summarized in Table 2 for the FM1 best focus position

at 7493.3 mm and its nominal focus position at 7500 mm. According to the simulation, the best focus position is nominal i.e equals 7500 mm while best focus measurements were performed at a -6.7 mm intrafocal shift. This focus shift remains unexplained. Indeed, the mirror numerical model does not contain absolute shell dimensions but deviation with respect to reference profiles. The absolute shell dimensions are taken from the optical design. The discrepancy between measured and simulated Full Width Half Maximum (FWHM), Half Energy Width (HEW) and 90 percent Energy Width (90W) is lower than 1.5 arcsec. Model accuracy, diffraction effects at 58 nm or UV collimator image quality are candidate explanations for the FWHM underestimate in the simulation with a 22.5 microns CCD pixel size. The discrepancy between the simulated and measured HEW are related to the inability for the model to account for the triangular shape of PSF. On the contrary, the PSF wings which are induced by mirror roll-off close to the edges and to the parabola/hyperbola intersection plane are well simulated. Indeed, the simulation accuracy of the encircled energy function is of the order of 1 percent above 20 arcsec radius.

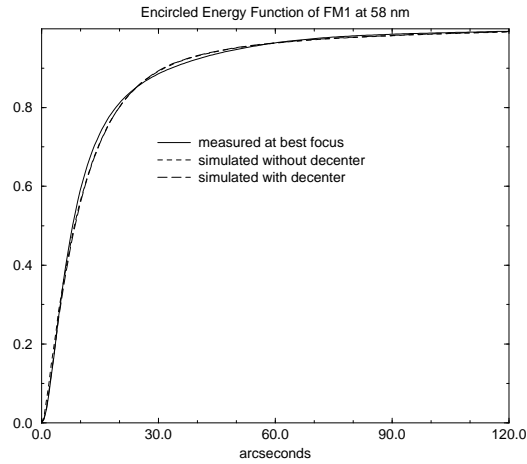


Figure 7. encircled energy function of XMM FM1 mirror module at 58nm

Table 2. Comparison between EUV measured and simulated image quality

Image Quality	Measured Best Focus	Measured F=7500mm	Simulated F=7500mm
FWHM (arcsec)	6.7	7.2	5.2
HEW (arcsec)	15.8	17.2	17.2
90W (arcsec)	62.3	67.1	62.7

4.2. X-ray Pencil Beam Tests

The CSL vertical test facility also provides a vertical x-ray channel which can be used to perform pencil beam tests on any single mirror of an integrated XMM mirror module. An x-ray pencil beam test was performed on the smallest FM1 mirror. Angle resolved scatter measurements indicate that the scattering contribution is negligible at 1.5 keV but is significant in the wing of the point spread function at 8 keV. The measured angle resolved scatter of mirror 58 was first compared with a best fit analytical simulation using the Rayleigh Rice theory. The core was modeled by a Gaussian having a 6 arc-second RMS slope error and various PSD description were used to matched the measured angle resolved scatter. An accurate fit is obtained when the wings are simulated using two fractal power spectral densities. The PSD constants and slope indices are $1.2 \times 10^{-8} \mu\text{m}^2 \text{ mm}$ and 0.5 respectively below 70 mm^{-1} spatial

frequency and $4.4 \times 10^{-6} \mu\text{m}^2 \text{ mm}$ and 1.9 above. Figure 5 compares the inferred surface power spectral density from the best fit angle resolved scatter with the average power spectral density of mirror 58 as measured by the microscope interferometer. The good match between the two curves indicates that the increases of the PSD slope at high frequencies is real and is not an artifact of the profilometer transfer function. A comparison between the measured and simulated angle resolved scatter of mirror 58 using the surface roughness metrology data is given in figure 8. Based on this analysis, the numerical model of the mirror module makes use of the average of the measured power spectral density of all mirrors.

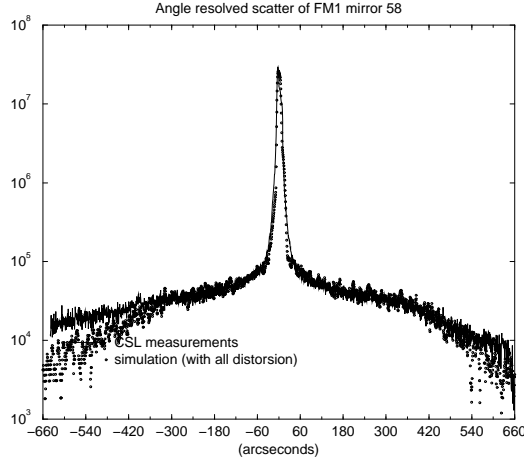


Figure 8. angle resolved scatter of mirror 58 at 8 keV

4.3. Measurements of the X-Ray Image Quality

After environmental and EUV test at CSL, the XMM Mirror Modules are sent to the PANTER facility¹⁶ for x-ray calibration under vacuum. The facility consists of a source chamber and an instrument test chamber connected by a tube of 130 meter length. The instrument test chamber is 13 meter long and has a diameter of 3.5 meters. It is equipped with an optical bench which hosted the FM1 mirror module. In its image plane, two detectors were mounted on a manipulator. These were the engineering model of the ROSAT Position Sensitive Proportional Counter (PSPC) and a Charge Coupled Device (CCD) camera provided by the University of Leicester. The PSPC which has a 37 arcmin diameter field of view was used for the characterization of the PSF wings. The smaller CCD detector probed the core of the point spread function with higher spatial resolution. The calibration tests at PANTER complement the CSL EUV tests by providing a full aperture illumination in x-ray with however some limitations. Because of the finite source distance, the first ten centimeters of the mirror parabola do not contribute to the image formation by double reflections. In addition, a few millimeters of the mirror surface near the parabola to hyperbola intersection plane is shadowed due to the dense packing geometry of the XMM mirror nest. Finally, the mirrors operate under a higher grazing angle with respect to infinite source distance which significantly effect their reflectivity at high energy. The spherical aberration induced by the finite source distance is however negligible.

Calculation of the PSF radial and encircled energy distribution have been performed with the ray tracing code including simulation of x-ray surface scattering from surface power spectral density measurements. According to simulation, the best focus position is nominal i.e equals 7981 mm while measurements indicate an intrafocal shift in agreement with CSL measurements. Figure 9 compares the simulated radial point spread function with the radial energy distribution of the FM1 and FM2 point response measured at 1.5 keV with the CCD. The radial energy distribution were normalized to maximum. Simulations of the radial energy distribution slightly loses accuracy in the far wings where the surface brightness has dropped by 4 to 5 orders of magnitude. This however does not effect the measurement accuracy of the encircled energy function. Figure 10 compares the measured and simulated

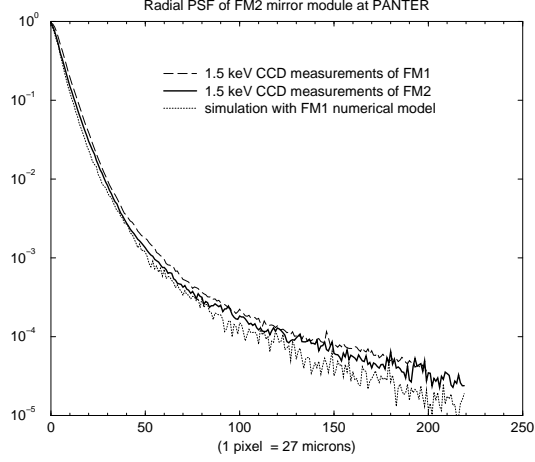


Figure 9. 1.5 keV PSF of FM1 and FM2 mirror module at PANTER (CCD measurement)

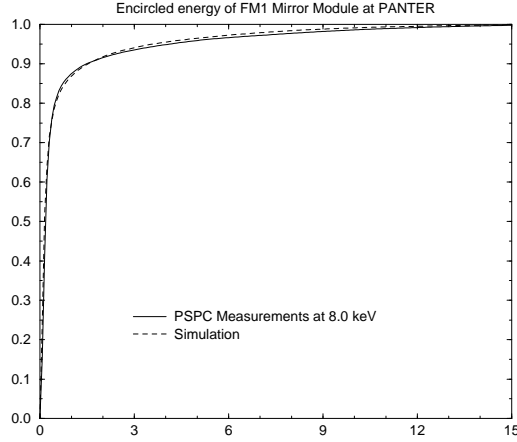


Figure 10. 8 keV encircled energy function of XMM FM1 mirror module at PANTER (PSPC measurements)

encircled energy distribution of the FM1 point spread function measured at 8 keV with the PSPC. The encircled energy function was normalized to 1 at a radius of 15 arcmin corresponding to the overall field of view of the EPIC camera. Simulation and measurement agree to better than 2 percent accuracy. A comparison between measurements and simulation is summarized in Table 3 at four different energies. The simulations provide a better fit to the CCD measurements in the core of the point spread function due to the decreasing spatial resolution of the PSPC with energy from 6.7 arcsec at 1.5 keV to 16.0 arcsec resolution at 8 keV. Table 3 shows that the simulation underestimates the 90 percent energy width at 4.5 and 6.4 keV. This translates into a difference between the measured and simulated encircled energy function of only 2 percents in the PSF wings.

Figure 11 visualizes the FM1 mirror module PSF measured with the CCD at 8 keV for off-axis angles of 7, 14 and 21 arcmin at different azimuths. A slight azimuthal dependence of the PSF shape is seen at large off-axis which

reduces the simulation accuracy of the off-axis encircled energy function. The agreement between the measured and simulated encircled energy function at 1.5 keV is 5 percent at 30 arcsec from the PSF center at an off-axis angle of 7 arcmin.

Table 3. Measurements and simulations of the FM1 image quality

Energy	Off-axis angle	FWHM (CCD)		HEW (CCD)		90W (PSPC)	
		meas. (arcsec.)	sim. (arcsec.)	meas. (arcsec.)	sim. (arcsec.)	meas. (arcsec.)	sim. (arcsec.)
1.5 keV	0 arcmin	7.6	6.0	15.2	14.0	60	59
	7 arcmin	7.3-8.2	6.2	16.8-18	16.3	67-77	61
	14 arcmin	7.7	6.4	21.2	18.4	87	68
	21 arcmin	7.8	6.9	32.6	30.5	118	96
4.5 keV	0 arcmin	7.6	6.0	15.6	14.8	146	105
6.4 keV	0 arcmin	9.9	7.2	15.3	15.3	207	164
8.0 keV	0 arcmin	7.1	4.0	14.5	15.8	181	181

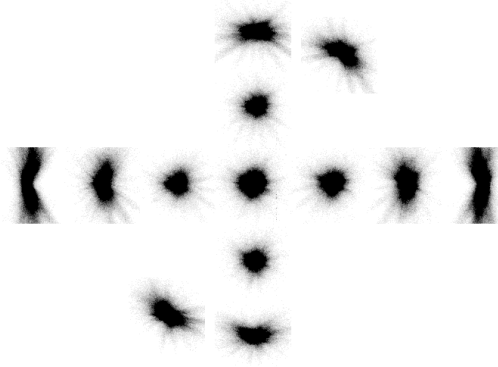


Figure 11. CCD off-axis PSF of FM1 Mirror Module at PANTER (8.0 keV)

5. CONCLUSIONS

The characterization of the mirror modules PSF is an important calibration task of the XMM mission payload. During the mission operation phase, it will be used by the science analysis software for source detection or filtering, selection of photometric extraction windows, background subtraction, detector pile-up correction, correction from scatter losses and possibly image restoration. However, in-orbit calibration of the mirror module point response on e.g stellar coronae will be limited in accuracy by spacecraft jitter, detector sampling and pile-up effect or statistical noise in the PSF core and by the x-ray background level in the PSF wings. The calibration therefore relies on the ability for the mirror software model to extrapolate on-ground calibration measurements to in-orbit operation conditions. The calibration approach performed on-ground on the first flight mirror module has demonstrated that the mirror figuring errors and the surface roughness measurement in the workshop can be use to simulate the response of the

FM1 mirror modules to a sufficient accuracy. The model has been validated by x-ray pencil beam tests and full aperture tests performed either in EUV with a collimated beam or in x-ray with a finite source distance. These tests indicate that the encircled energy function in orbit can be characterized to an accuracy of about 2 percent for an on-axis source. This accuracy meet the initial calibration goal.

6. ACKNOWLEDGMENTS

We wish to congratulate the MEDIALARIO mirror manufacturing team for the outstanding performance of the XMM flight mirror modules. Many thanks go to our colleagues from the PANTER and CSL test facilities for their dedication to the calibration tests of the XMM mirror modules.

7. REFERENCES

- 1 F. Jansen, "XMM Observatory: a scientific and technical overview", These Proceedings.
- 2 Ph. Gondoin, D. de Chambure, K. van Katwijk, Ph. Kletzkine, D. Stramacicioni, B. Aschenbach, O. Citterio, R. Willingale, "The XMM Telescope", SPIE Proc.2279, pp.86-100, 1994.
- 3 D. de Chambure, R. Laine, K. van Katwijk, J. van Casteren, P. Glaude, "Status of the x-ray flight mirror production for the ESA XMM spacecraft", SPIE Proc.3114, pp. 113-124, 1997
- 4 A.D.Holland, M.J.L.Turner, A.F.Abbey, P.J. Pool, "MOS CCDs for the EPIC on XMM", SPIE Proc.2808, pp. 414-420, 1996
- 5 N. Meidinger, H.W. Brauninger, R. Hartmann, G. Hartner, N. Krause, E. Pfeffermann, C. Reppin, G. Schwaab, L. Struder, J. Trumper, P. Holl, J. Kemmer, S. Krisch, H. Soltau, C. van Zanthier, D. Hauf, R. Richter, "PN-CCD detector for the European Photon Imaging Camera on XMM", SPIE Proc.2808, pp. 492-503, 1996
- 6 A.C.Brinkman, H.J.M.Aaarts, A.J.F.den Boggende, L.Dubbeldam, J.W.den Herder, J.S.Kaastra, P.A.J.de Korte, R.Mewe, C.J.Hailey, S.M.Kahn, F.B.S.Paerels, G.Branduardi-Raymont, J.V.Bixler, K.Thomsen, A.Zehnder, "Reflection Grating Spectrometer on-board XMM", SPIE Proc.2808, pp. 463-480, 1996
- 7 R. Much, D. Lumb, M.S. Cropper, R. Hunt, K.O. Mason, F.A. Cordova, T. Sasseen, C. Ho, W. Priedhorsky, C.Jamar, E. Antonello, "The Optival/UV Monitor on the X-ray Multi Mirror Mission",Proceedings of the Conference " Ultraviolet Astrophysics, Beyond the IUE Final Archive", Sevilla, Spain, 11-14 November 1997, ESA SP-413, pp.815, 1998
- 8 B. Aschenbach, H. Brauninger, SPIE Proc. 1742, pp. 284-294, 1992
- 9 Ph. Gondoin, K. van Katwijk, B. Aschenbach, N. Schulz, R. Borret, H. Glatzel, O. Citterio, R. Willingale, "XMM Telescope Development", EOS/SPIE Proc. 2209, PP438-450, 1994.
- 10 P.Z. Takacs and E.L. Church,"Figure and finish of grazing incidence mirrors", Nucl. Inst. Meth. Phys. Res. A291, 253, 1990
- 11 B.L. Henke, E.M Gullikson E.M., J.C Davis, Atomic Data and Nuclear Data Tables, July 1993, Vol 54
- 12 D.W. Lynch and W.R. Hunter, "Handbook of Optical Constants of Solids", ed. E.D. Palik, Academic Press, Orlando, 1985
- 13 Ph. Gondoin, B. Aschenbach , H. Brauninger , D. de Chambure, J.P. Colette, R. Egger, K. van Katwijk, D. Lumb, A. Peacock, Y.Stockmann, J.P. Tock, R. Willingale, " Simulation of the XMM Mirror Performance based on Metrology Data",SPIE Proc. 2808, pp. 390-401, 1996
- 14 P.Hariharan, B.F. Oreb, T. Eiju, "Digital Phase-Shifting Interferometry, a Simple Error Compensating Phase Calculation Algorithm", Appl. Opt. 26, pp2504-2505, 1987.
- 15 Y. Stockman, J.P. Tock, D. de Chambure, Ph. Gondoin, "XMM flight mirror module environmental and optical testing", These proceedings.
- 16 R. Egger, B. Aschenbach, H. Brauninger, W. Burket, T. Dohring, A. Oppitz," X-ray calibration of the XMM flight mirror modules at the PANTER test facility", These proceedings.